Letter

Type-II Dirac point in $RbAg_5Se_3$

Huanzhao Lv,[1] Zhenwei Wang,[1] Qiubo Cheng,[1] Wei Zhang,[2,*] and Rui Yu[1,†]

[1]*School of Physics and Technology, Wuhan University, Wuhan 430072, China*

[2]*Fujian Provincial Key Laboratory of Quantum Manipulation and New Energy Materials, College of Physics and Energy, Fujian Normal University, Fuzhou 350117, China*

(Received 27 January 2021; revised 17 May 2021; accepted 8 June 2021; published 24 June 2021)

Using first-principles calculations and low-energy effective model analysis, we propose that silver selenide-based $RbAg_5Se_3$ compound is an ideal type-II Dirac semimetal. There is a pair of Dirac points appearing at about 25.68 meV below the Fermi energy. The Dirac points existing on the k_z axis are protected by C_{4z} rotation symmetry in addition to $\mathcal{PT}$ symmetry. Meanwhile, the system is also characterized by a nontrivial $\mathbb{Z}_2$ topological invariant. The long clean Fermi arcs exist on the (010) surface, connecting the projections of the Dirac points. In addition, the Landau levels of the type-II Dirac points under magnetic field are also calculated. Our discovery not only adds one promising candidate into the type-II Dirac semimetals family but also provides an ideal platform for the study of topological phase transitions.

DOI: 10.1103/PhysRevB.103.L241115

I. INTRODUCTION

Topological semimetals with unique electronic structure and transport properties have been extensively studied recently [1–17]. They are characterized by the band-touching points between conduction and valence bands near the Fermi energy in the Brillouin zone (BZ). Considering the bands degeneracy, topological semimetals can be classified as Dirac semimetals [18–20] with fourfold degenerate band touching points, Weyl semimetals [21–23] with twofold degenerate band touching points, multiply degenerate (three-, six-, eightfold) semimetals [24–27], and nodal line semimetals [28–31]. Moreover, according to the crossing types and Fermi surface around Dirac/Weyl points, Dirac/Weyl semimetals can be classified as two types: Type-I and type-II. The type-I fermions have a counterpart in the high-energy physics because the low-energy states can be described by the standard Dirac/Weyl equation, and the Fermi surfaces are pointlike lying at the Fermi level. As for type-II fermions, the Lorentz symmetry is not maintained and the dispersion cone occurs in a overtilted form, in which the electron and hole pockets can coexist with a contourlike Fermi surface. Among these topological semimetals, the Dirac topological phases are often protected by crystal symmetry and time-reversal symmetry. The novel Dirac semimetal states can lead to different phase transitions by symmetry breaking. If the time-reversal symmetry is broken by external magnetic field or magnetic doping, the Dirac states can transit into Weyl states. Also, the crystal symmetry protecting Dirac states can be broken by external strain; the Dirac semimetal can transit into a topological insulator or a trivial insulator. Therefore, Dirac semimetal can provide an ideal platform to study various quantum phase transitions.

Type-II Dirac semimetals have been reported to host many unusual properties, such as topological Lifshitz transitions [32], angle-dependent chiral anomaly [1], and even topological superconductivity [33,34]. Up to now, a lot of Dirac materials have been predicted and confirmed, but only a few three-dimensional (3D) type-II Dirac semimetal materials ($PtSe_2$ class [32], YPd_2Sn class [33], $ZrInPd_2$ class [34], RMgBi [35], and VAl_3 [36]) have been discovered. However, these materials are not perfect for further study. For example, topological properties of VAl_3 families are characterized by nontrivial mirror Chern number $n_M = 2$, but their Fermi surfaces are not so clean for experimental confirmation. Among the type-II Dirac materials, group-X Pt and Pd-based dichalcogenides $PtSe_2$ class have been mainly studied by experiments via angle-resolved photo-emission spectroscopy (ARPES) measurements and quantum oscillation measurements [37–42]. Unfortunately, their Dirac points are far below the Fermi level, about 0.6 eV in $PdTe_2$, 0.8 eV in $PtTe_2$, and 1.2 eV in $PtSe_2$. Only $NiTe_2$ [43,44] has recently been reported to have a pair of type-II Dirac nodes approaching the Fermi level.

As most electronic properties of metals are determined solely by the low-energy states around the Fermi energy, we would like to discover topological semimetals with clean Fermi surface and topological charge around the Fermi level. In this work, based on the detailed first-principles calculations, we reveal that the existing material $RbAg_5Se_3$ compound is an ideal type-II Dirac semimetal material. Without spin-orbit coupling (SOC), there is a pair of triple points on the k_z axis. When the SOC effect is included, each triple degenerate point transits into a type-II Dirac point and a nondegenerate band. The Dirac points locate at 25.68 meV below the Fermi energy and are favorable for experimental observation. The corresponding surface states and arcs are clean, and

*Corresponding author: zhangw721@163.com

†Corresponding author: yurui@whu.edu.cn

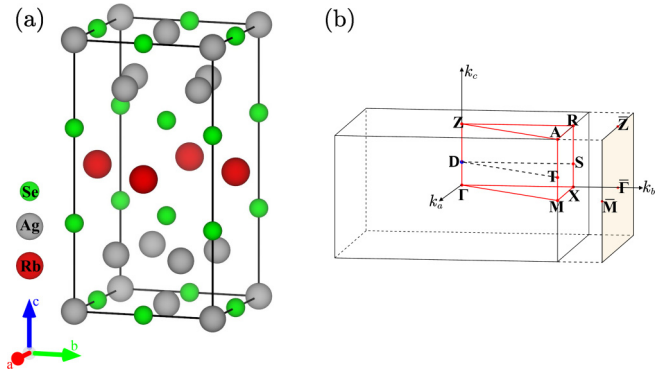

FIG. 1. (a) The crystal structure of $RbAg_5Se_3$; (b) high-symmetry lines in the BZ and the BZ projection plane onto the (010) direction.

we found that the electron and hole bulk states touch at the Dirac points, leading to long Fermi arcs. Through symmetry analysis we construct the low-energy effective model and verify that the Dirac points protected by the C_{4v} point group and time-inversion ($\mathcal{PT}$) symmetry robustly exist on the k_z axis. When magnetic field is applied along the k_z direction, there is an almost $n = 0$ flat Landau level lying in the k_z direction. Our discovery not only enlarges the family of the type-II Dirac semimetals but also paves the way for the quantum study of topological phase transitions.

II. CRYSTAL STRUCTURE AND NUMERICAL METHODS

The experimental synthesized $RbAg_5Se_3$ compound with space group $P4/nbm$ (No. 125) is studied in our work [45]. It crystallizes in the tetragonal layered structure with a single Rb layer located between two silver selenide slab layers as shown in Fig. 1(a), and the separated up and down silver selenide slabs are identical due to the inversion symmetry. The experimental lattice parameters and atom positions are summarized in Table I. As the optimized structural parameters are within 1% of the corresponding experimental data, we choose the experimental data for calculations in this paper. The symmetry operations of the space group have five generators: Identity E, inversion $\mathcal{P}$, and three rotations along the principle axes with each followed by a translation [in units of (a, a, c)]: $\widetilde{C}_{2z} = \{C_{2z}|(\frac{1}{2}, \frac{1}{2}, 0)\}$, $\widetilde{C}_{4z} = \{C_{4z}|(\frac{1}{2}, 0, 0)\}$, and $\widetilde{C}_{2y} = \{C_{2y}|(\frac{1}{2}, 0, 0)\}$. The time-reversal symmetry $\mathcal{T}$ is also preserved in our system.

TABLE I. Lattice parameters and atom positions of $RbAg_5Se_3$.

a(Å)	b(Å)	c(Å)	α	β	γ
6.0814	6.0814	11.112	90°	90°	90°
	Site	Wyckoff	x	y	z
1	Rb	2d	0.750	0.250	0.500
2	Ag1	2a	0.250	0.250	0.000
3	Ag2	8m	0.454	0.546	0.190
4	Se1	2d	0.750	0.250	0.000
5	Se2	4g	0.250	0.250	0.324

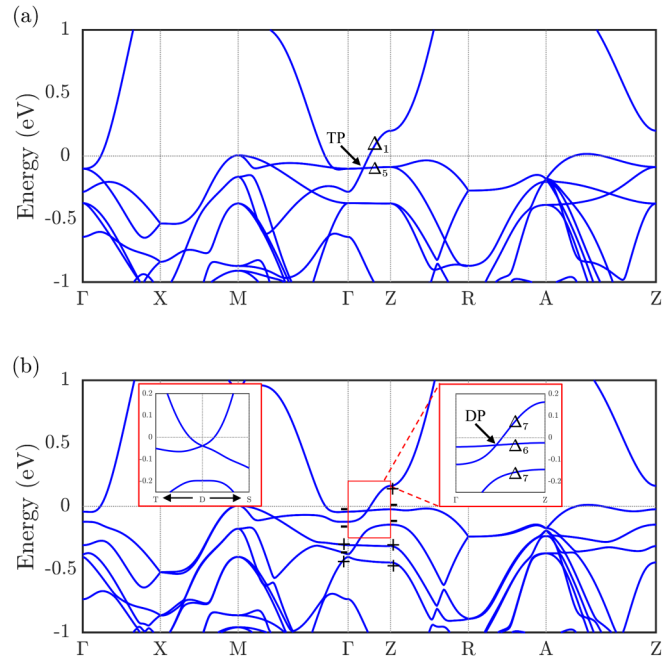

FIG. 2. (a) Bulk band structures with a triple-degenerate point (TP) near the Fermi energy along the Γ-Z line for the no-SOC case. (b) Bulk band structures with a Dirac point (DP), which is much closer to the Fermi energy for the SOC case; the insets are enlarged bands dispersion around the DP in Γ-Z direction (right) and in T-D-S directions (left) of BZ. The signs "+" and "−" are the parities of the corresponding bands on the high-symmetry points Γ and Z.

We perform density-functional theory (DFT) calculations to investigate the band structures of $RbAg_5Se_3$ by using projector-augmented plane-wave method [46] as implemented in the Vienna *ab initio* simulation package [47,48]. The generalized gradient approximation (GGA) in Perbew-Burke-Ernzerhof exchange-correlation functional is used. The cutoff energy with plane-wave basis set is 500 eV and the Monkhorst-Pack mesh of Γ-centered $11 \times 11 \times 6$ k-points is applied for structure relaxation [49]. The nonlocal Heyd-Scuseria-Ernzerhof (HSE) hybrid functional calculations [50] are also used to check the band structure. The tight-binding model is obtained by constructing maximally localized Wannier functions (WFs) [51–53], which are generated from 5s, 4d orbitals of Ag and 4p orbitals of Se. Topological surface states are calculated by using the iterative Green function method [54] as implemented in the WannierTools package [55].

III. RESULTS

A. Band structures

Based on the DFT calculations, the band structures of bulk $RbAg_5Se_3$ without and with SOC are shown in Fig. 2. That conduction and valence bands cross each other along the Γ-Z line reveal it is a semimetal. This is well consistent with the experimental results that $RbAg_5Se_3$ is a weakly metallic conductor [45]. Our orbital analysis shows that the bands around the Fermi level mainly consist of Ag 4d and Se 4p orbitals. As clearly illustrated in Fig. 2(a), without SOC, the band

TABLE II. Character table for the point group C_{4v} along the Γ-Z direction. Only the related representations without SOC (Δ_1 and Δ_5) and with SOC (Δ_6 and Δ_7) are given below.

C_{4v}	E	C_{4z}	C_{2z}	M_x	M_{110}
Δ_1	1	1	1	1	1
Δ_5	2	0	−2	0	0
Δ_6	2	$\sqrt{2}$	0	0	0
Δ_7	2	$-\sqrt{2}$	0	0	0

crossing point near the Fermi level is triply degenerate along the Γ-Z line. The crossing bands belong to 1D representation Δ_1 and 2D representation Δ_5 of C_{4v} point group as described in Table II; the Δ_1 band is mainly composed of Se p_z orbitals, while the Δ_5 is mainly composed of Se $p_x + p_y$ orbitals. Finally, these two bands can simply cross each other, forming a stable triple degenerate point without any hybridization.

Due to the strong SOC effect of $RbAg_5Se_3$ compound, along the Γ-Z line, the originally single Δ_1 band transits into Δ_7 states, while the twofold degenerate Δ_5 band splits into upper Δ_6 and lower Δ_7 states without any crossings as shown in the enlarged right panel of Fig. 2(b). Interestingly, two bands near the Fermi energy in the Γ-Z line hybridize and open a gap, because they have the same irreducible representation (IR) Δ_7 of C_{4v}, while the bands having different IRs with opposite rotation character of C_{4z} (Table II) can cross each other. Because of the coexistence of inversion and time-reversal symmetries in this system, all the bands are double degenerate and symmetric in k and $-k$ points. The crossing point is a quadruply degenerate point and can be protected from the gap opening by any perturbation as long as the C_{4z} symmetry is satisfied [56]. Around the fourfold degenerate point, the band dispersion of Δ_6 is almost flat, while the Dirac cone is a little overtilted along the Γ-Z line [right inset in Fig. 2(b)], but not in the xy plane [left inset in Fig. 2(b)]. Obviously, this is the main feature of type-II Dirac semimetals [32,36]. Carefully scanning the whole BZ, our first-principles calculations show that there exists a pair of symmetry-protected Dirac points located at $k_D = (0, 0, \pm 0.1886\frac{2\pi}{c})$. The Dirac points in $RbAg_5Se_3$ are at $E_D = -25.68$ meV, which are much closer to the Fermi level than those of Dirac points in other reported type-II Dirac semimetals. Thus, it is an ideal type-II Dirac material for experimental study.

B. Surface states and topological properties

To further reveal the topological properties of $RbAg_5Se_3$, we investigate the evolution of Wannier charge centers (WCC). In the presence of SOC, the system is fully gapped both in the $k_z = 0$ and $k_z = \pi$ plane. These planes can be considered as 2D systems with $\mathcal{T}$ symmetry, so we can define the $\mathbb{Z}_2$ invariant on the planes [18]. We trace the evolution of WCC on these planes and find that the $\mathbb{Z}_2$ invariant is 1 in $k_z = 0$ plane while it is 0 in $k_z = \pi$ plane by using the Wilson loop method [57], as shown in Figs. 3(c) and 3(d). Thus, the Dirac points are topological protected by C_{4z} rotation and $\mathcal{PT}$ symmetry, and the system is with a nontrival $\mathbb{Z}_2$ invariant.

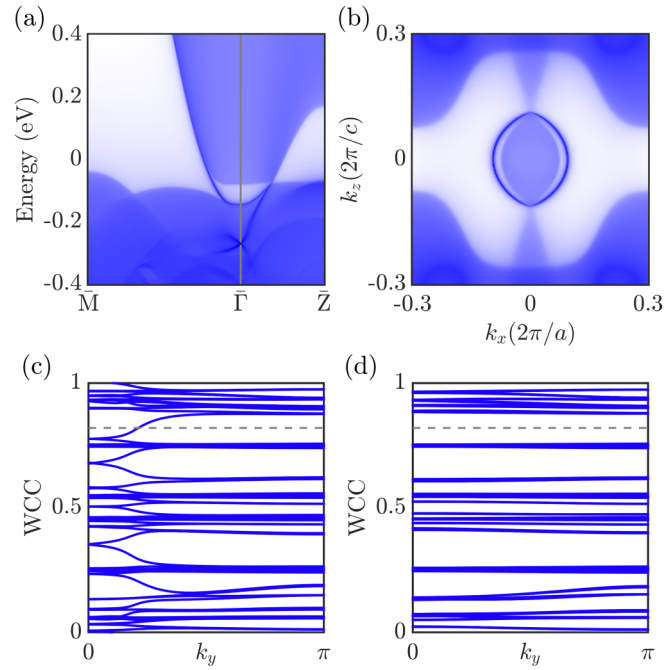

FIG. 3. (a) Surface states along the $\bar{M}$-$\bar{\Gamma}$-$\bar{Z}$ lines in (010) surface BZ. (b) The Fermi arcs connect the projections of Dirac points on the (010) surface with constant energy at E_D. (c), (d) Evolution of WCCs in the $k_z = 0$ and $k_z = \pi$ planes, respectively. They exhibit odd number crossings with nontrivial $\mathbb{Z}_2 = 1$ in the $k_z = 0$ plane, while even number crossings with trivial $\mathbb{Z}_2 = 0$ in the $k_z = \pi$ plane.

This is similar to the well-known type-I Dirac semimetal Cd_3As_2 [19].

One of the features of topology in crystals is the existence of exotic surface states. We further calculate the (010) pro-

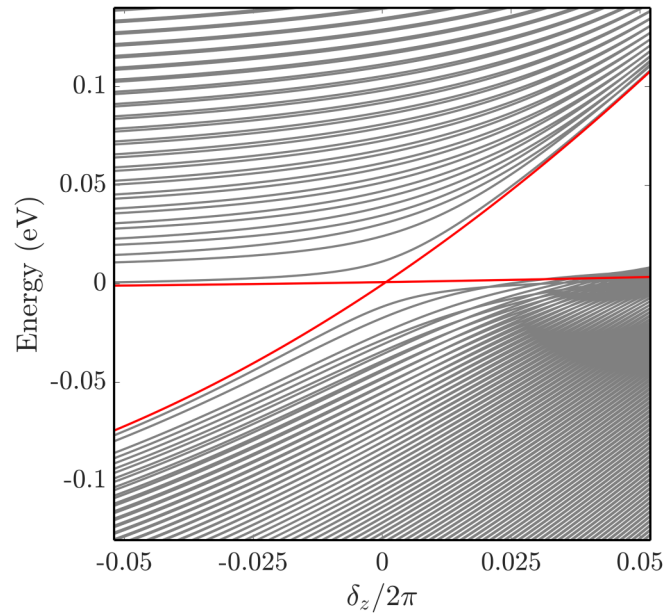

FIG. 4. Landau levels dispersion around type-II Dirac point of $RbAg_5Se_3$ with a magnetic field $B = 5$ T along the k_z axis. The red lines are $n = 0$ Landau levels in the magnetic field.

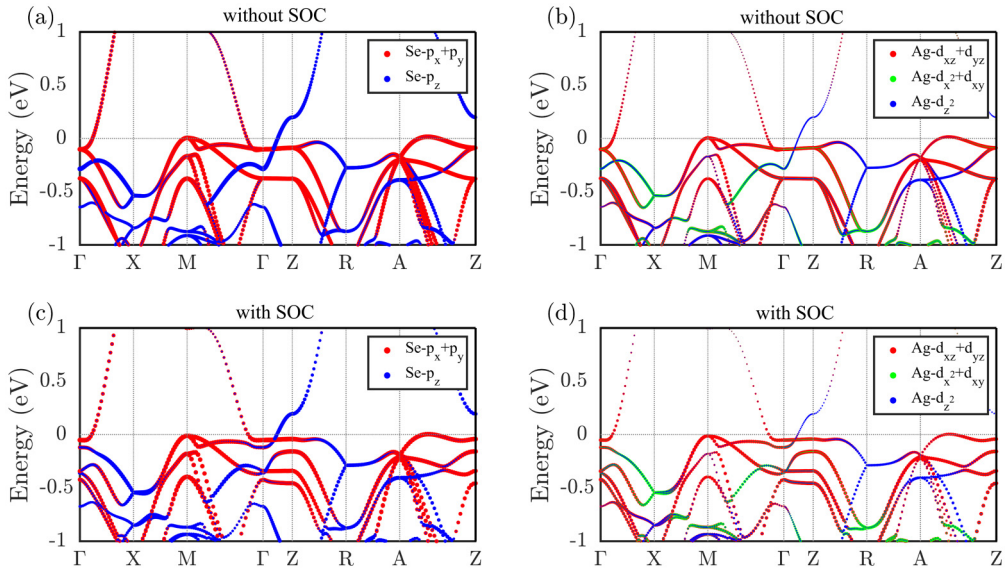

FIG. 5. The orbital-resloved band structures of $RbAg_5Se_3$. (a) and (b) are Se 4p and Ag 4d orbital projections respectively when SOC effect is not considered. (c) and (d) are Se 4p and Ag 4d orbital projections respectively when SOC effect is turn on.

jected surface states based on the tight-binding Hamiltonian constructed from WFs. It is clear that the conduction bulk states and valence states touch at the Dirac points, where the topological surface states emerge as shown in Fig. 3(a). Also in Fig. 3(b), the long surface Fermi arcs connect the projections of two Dirac points at $k_D = (0, 0, \pm\ 0.1886\frac{2\pi}{c})$. It shows that the bulk states surrounded by Fermi arcs are the hole states while the outer ones are electron states. They are touching at the two Dirac points. This is another feature of type-II Dirac semimetals [32].

C. The k · p model Hamiltonian for the bulk type-II Dirac point

In order to understand the forming mechanism of type-II Dirac states in $RbAg_5Se_3$ when SOC is included, an extensive symmetry is analyzed. The first-principles calculations show that the Dirac node is formed through the crossing of $\Delta_6(s = \pm\frac{1}{2})$ and $\Delta_7(s = \pm\frac{3}{2})$ states of C_{4v} little group in the Γ-Z line [Fig. 2(b)], and the model Hamiltonian is constructed based on these two bases. The generators of C_{4v} point group are the fourfold rotation C_{4z} along [001] direction and a mirror plane M_y in [010] direction. The Dirac points are also protected by $\mathcal{PT}$ symmetry. According to Table II, these symmetry operations on these bases can be represented as $C_{4z} = diag(e^{-i\pi/4}, e^{i\pi/4}, e^{-i3\pi/4}, e^{i3\pi/4})$, $M_y = -i\tau_0\sigma_x$, and $\mathcal{PT} = -i\tau_0\sigma_y\mathcal{K}$ (where $\mathcal{K}$ is complex conjugate operator and $\boldsymbol{\tau}$ and σ denote the orbital and spin degree of freedom, respectively). Actually, the model Hamiltonian constrained by these operations can be described as:

$$\begin{aligned} C_{4z}H_D(k_x, k_y, k_z)C_{4z}^{-1} &= H_D(k_y, -k_x, k_z) \\ M_yH_D(k_x, k_y, k_z)M_y^{-1} &= H_D(k_x, -k_y, k_z) \\ (\mathcal{PT})H_D(k_x, k_y, k_z)(\mathcal{PT})^{-1} &= H_D(k_x, k_y, k_z). \end{aligned} \tag{1}$$

Using the basis given above, we can obtain the minimal four-band Hamiltonian near the Dirac point, up to the quadratic order in $\mathbf{k}$:

$$H_D(\mathbf{k}) = \begin{pmatrix} \epsilon_1(\mathbf{k}) & 0 & A(\mathbf{k})) & B(\mathbf{k}) \\ & \epsilon_1(\mathbf{k}) & -B^*(\mathbf{k}) & A^*(\mathbf{k}) \\ & & \epsilon_2(\mathbf{k}) & 0 \\ \dagger & & & \epsilon_2(\mathbf{k}) \end{pmatrix}, \tag{2}$$

with $\epsilon_1(\mathbf{k}) = a_1k_+k_- + b_1k_z^2 + c_1k_z$, $\epsilon_2(\mathbf{k}) = a_2k_+k_- + b_2k_z^2 + c_2k_z$, $A(\mathbf{k}) = ik_-(d_1 + d_2k_z)$, $B(\mathbf{k}) = i(d_3k_-^2 + d_4k_+^2)$ ($k_\pm = k_x \pm ik_y$). The parameters mentioned above are real numbers. Thus, a Dirac point at $\mathbf{k} = \mathbf{0}$ can be denoted. The above parameters are determined by fitting the energy dispersion of effective Hamiltonian with first-principles results. These parameters are $a_1 = 5.1\,\text{eVÅ}^2$, $a_2 = 0.5\,\text{eVÅ}^2$, $b_1 = 0.20\,\text{eVÅ}^2$, $b_2 = 32.2\,\text{eVÅ}^2$, c_1=0.08 eVÅ, c_2=3.2 eVÅ, d_1=0.41 eVÅ, $d_2 = 0.1\,\text{eVÅ}^2$, $d_3 = 4.0\,\text{eVÅ}^2$, $d_4 = 4.0\,\text{eVÅ}^2$.

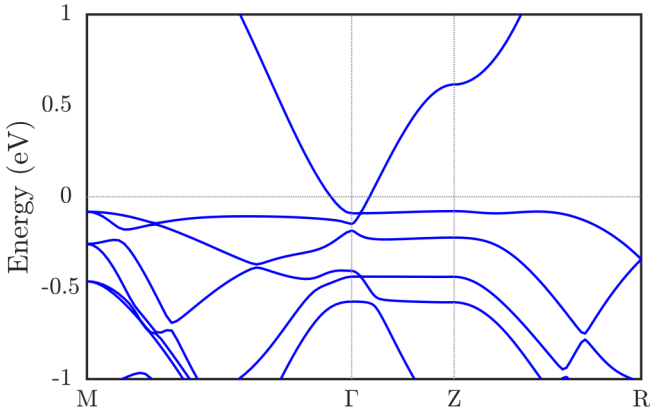

FIG. 6. The HSE calculated band structures of $RbAg_5Se_3$ along the high-symmetry line M − Γ − Z − R in the BZ.

D. Landau level spectrum analysis

Dirac semimetals have many exotic transport properties when the magnetic field is applied. Usually, these transport properties are related to the Landau levels contributed by the Dirac points. For the type-II Dirac semimetals, the Landau levels will collapse due to the opening quasiclassical orbitals for the field in the xy plane [36]. Therefore, we deduce that the Landau levels will collapse when the magnetic field is applied in the xy plane. Here, we only consider a uniform magnetic field applied along the z direction with Landau gauge $\mathbf{A} = (-By, 0, 0)$. Under the Peierls substitution, the wave vector $\mathbf{k}$ becomes $\boldsymbol{\pi} = \mathbf{k} + \frac{e}{\hbar}\mathbf{A}$. We can rewrite the conjugate momenta as $\pi_x = \frac{1}{\sqrt{2}l_c}(a^\dagger + a)$, $\pi_y = \frac{-i}{\sqrt{2}l_c}(a^\dagger - a)$ with magnetic length $l_c = \sqrt{\frac{\hbar}{eB}}$. Near the Dirac point, the above the $\mathbf{k}\cdot\mathbf{p}$ Hamiltonian (only keep the kinetic and linear terms) under the magnetic field is:

$$H_{eff} = \begin{pmatrix} M_1 & 0 & \frac{i\sqrt{2}}{l_c}d_1 a & 0 \\ & M_1 & 0 & -\frac{i\sqrt{2}}{l_c}d_1 a^\dagger \\ & & M_2 & 0 \\ \dagger & & & M_2 \end{pmatrix}, \qquad (3)$$

with $M_1 = \frac{2a_1}{l_c^2}a^\dagger a + b_1\delta_z^2 + c_1\delta_z$, $M_2 = \frac{2a_2}{l_c^2}a^\dagger a + b_2\delta_z^2 + c_2\delta_z$. The Landau levels contributed by the type-II Dirac point at $(0, 0, k_D)$ are clearly observed in Fig. 4. Each Dirac point will generate two chiral modes corresponding to the two degenerate Weyl points. In addition, there is an almost flat chiral mode along the k_z axis which is the same as the band structure results. This is a key character of the type-II Dirac point in bulk $RbAg_5Se_3$, which is the same as that studied in RbMgBi [35].

IV. DISCUSSIONS AND CONCLUSIONS

Finally, we remark that the nontrivial band topology of $RbAg_5Se_3$ is the same as that in Materiae, an online database of topological material classification [58]. The database qualitatively informs that it is a high-symmetry line semimetal with SOC interaction, while it is a high-symmetry point semimetal without SOC. However, the detailed information about topological feature and topological invariant of this type-II semimetal is not shown [59]. In this work, we systematically investigate the topological properties of $RbAg_5Se_3$ and propose that silver selenide-based $RbAg_5Se_3$ compound is a type-II Dirac semimetal through the first-principles calculations and low-energy effective $\mathbf{k}\cdot\mathbf{p}$ model analysis. Without SOC, it realizes a pair of triple degenerate points on the C_4 rotation axis. In the presence of SOC effect, $RbAg_5Se_3$ becomes a type-II Dirac semimetal with a pair of Dirac nodal points lying on the C_4 rotation axis. The type-II Dirac points are approaching the Fermi level with an energy level at -25.68 meV. The Fermi surface is clean and the corresponding long Fermi arcs are favorable for experimental observation. When applying a magnetic field, the main feature of the topological type-II Dirac semimetal is that there always exists an almost flat chiral mode very close to the Fermi level. The above results are hopeful for future verification by scanning tunneling spectroscopy and ARPES measurements.

ACKNOWLEDGMENTS

We thank Yi Jiang for helpful discussions. This work was supported by the National Key Research and Development Program of China (No. 2017YFA0303402 and No. 2017YFA0304700), and the National Natural Science Foundation of China (No. 11974076 and No. 11704117), and Natural Science Foundation of Fujian Province of China (No. 2018J06001). Numerical calculations presented in this paper have been performed on the supercomputing system in the Supercomputing Center of Wuhan University.

APPENDIX A: ORBITAL-RESOLVED BAND STRUCTURE

To better clearly illustrate the bands composition and how the type-II Dirac points are formed when SOC effect is turn on, the orbital-resloved band structures of $RbAg_5Se_3$ with Se 4p and Ag 4d orbitals are presented respectively in Fig. 5. We can see the bands around the Fermi level are dominated by Ag 4d and Se 4p orbitals. The valence and conduction bands cross along the Γ-Z line near the Fermi level are mainly consisted of Se p_z orbitals and Se $p_x + p_y$ orbitals.

APPENDIX B: HSE BAND STRUCTURES

In order to overcome the well-known band gap underestimation of the GGA calculation results, we also verify whether the type-II Dirac points of $RbAg_5Se_3$ is maintained when we use the HSE [50] exchange-correlation functional. The HSE band structure results in Fig. 6 show that the crossing of valance and conduction bands along the Γ-Z line confirms the system is a semimetal. This is the same as the results from the GGA calculation results.

[1] N. P. Armitage, E. J. Mele, and A. Vishwanath, Rev. Mod. Phys. **90**, 015001 (2018).
[2] S. Borisenko, Q. Gibson, D. Evtushinsky, V. Zabolotnyy, B. Büchner, and R. J. Cava, Phys. Rev. Lett. **113**, 027603 (2014).
[3] A. A. Burkov, M. D. Hook, and L. Balents, Phys. Rev. B **84**, 235126 (2011).
[4] A. A. Burkov and L. Balents, Phys. Rev. Lett. **107**, 127205 (2011).
[5] T. Bzdušek, Q. Wu, A. Rüegg, M. Sigrist, and A. A. Soluyanov, Nature **538**, 75 (2016).
[6] Q. D. Gibson, L. M. Schoop, L. Muechler, L. S. Xie, M. Hirschberger, N. P. Ong, R. Car, and R. J. Cava, Phys. Rev. B **91**, 205128 (2015).
[7] P. Hosur and X. Qi, C. R. Phys. **14**, 857 (2013).
[8] C.-X. Liu, P. Ye, and X.-L. Qi, Phys. Rev. B **87**, 235306 (2013).
[9] J. Ruan, S.-K. Jian, D. Zhang, H. Yao, H. Zhang, S.-C. Zhang, and D. Xing, Phys. Rev. Lett. **116**, 226801 (2016).

[10] J. Ruan, S.-K. Jian, H. Yao, H. Zhang, S.-C. Zhang, and D. Xing, Nat. Commun. **7**, 11136 (2016).

[11] A. A. Soluyanov, D. Gresch, Z. Wang, Q. Wu, M. Troyer, X. Dai, and B. A. Bernevig, Nature **527**, 495 (2015).

[12] D. T. Son and B. Z. Spivak, Phys. Rev. B **88**, 104412 (2013).

[13] Y. Sun, S.-C. Wu, M. N. Ali, C. Felser, and B. Yan, Phys. Rev. B **92**, 161107(R) (2015).

[14] P. Tang, Q. Zhou, G. Xu, and S.-C. Zhang, Nat. Phys. **12**, 1100 (2016).

[15] X. Wan, A. M. Turner, A. Vishwanath, and S. Y. Savrasov, Phys. Rev. B **83**, 205101 (2011).

[16] H. Wei, S.-P. Chao, and V. Aji, Phys. Rev. Lett. **109**, 196403 (2012).

[17] G. Xu, H. Weng, Z. Wang, X. Dai, and Z. Fang, Phys. Rev. Lett. **107**, 186806 (2011).

[18] Z. Wang, Y. Sun, X.-Q. Chen, C. Franchini, G. Xu, H. Weng, X. Dai, and Z. Fang, Phys. Rev. B **85**, 195320 (2012).

[19] Z. Wang, H. Weng, Q. Wu, X. Dai, and Z. Fang, Phys. Rev. B **88**, 125427 (2013).

[20] S. M. Young, S. Zaheer, J. C. Y. Teo, C. L. Kane, E. J. Mele, and A. M. Rappe, Phys. Rev. Lett. **108**, 140405 (2012).

[21] S.-M. Huang, S.-Y. Xu, I. Belopolski, C.-C. Lee, G. Chang, B. Wang, N. Alidoust, G. Bian, M. Neupane, C. Zhang, S. Jia, A. Bansil, H. Lin, and M. Z. Hasan, Nat. Commun. **6**, 7373 (2015).

[22] H. Weng, C. Fang, Z. Fang, B. A. Bernevig, and X. Dai, Phys. Rev. X **5**, 011029 (2015).

[23] B. Q. Lv, H. M. Weng, B. B. Fu, X. P. Wang, H. Miao, J. Ma, P. Richard, X. C. Huang, L. X. Zhao, G. F. Chen, Z. Fang, X. Dai, T. Qian, and H. Ding, Phys. Rev. X **5**, 031013 (2015).

[24] B. Bradlyn, J. Cano, Z. Wang, M. G. Vergniory, C. Felser, R. J. Cava, and B. A. Bernevig, Science **353**, aaf5037 (2016).

[25] H. Weng, C. Fang, Z. Fang, and X. Dai, Phys. Rev. B **94**, 165201 (2016).

[26] Z. Zhu, G. W. Winkler, Q. Wu, J. Li, and A. A. Soluyanov, Phys. Rev. X **6**, 031003 (2016).

[27] B. Q. Lv, Z.-L. Feng, Q.-N. Xu, X. Gao, J.-Z. Ma, L.-Y. Kong, P. Richard, Y.-B. Huang, V. N. Strocov, C. Fang, H.-M. Weng, Y.-G. Shi, T. Qian, and H. Ding, Nature **546**, 627 (2017).

[28] R. Yu, H. Weng, Z. Fang, X. Dai, and X. Hu, Phys. Rev. Lett. **115**, 036807 (2015).

[29] H. Weng, Y. Liang, Q. Xu, R. Yu, Z. Fang, X. Dai, and Y. Kawazoe, Phys. Rev. B **92**, 045108 (2015).

[30] H. Weng, X. Dai, and Z. Fang, J. Phys.: Condens. Matter **28**, 303001 (2016).

[31] J. Zhao, R. Yu, H. Weng, and Z. Fang, Phys. Rev. B **94**, 195104 (2016).

[32] H. Huang, S. Zhou, and W. Duan, Phys. Rev. B **94**, 121117(R) (2016).

[33] P.-J. Guo, H.-C. Yang, K. Liu, and Z.-Y. Lu, Phys. Rev. B **95**, 155112 (2017).

[34] C. Mondal, C. K. Barman, B. Pathak, and A. Alam, Phys. Rev. B **100**, 245151 (2019).

[35] C. Le, S. Qin, X. Wu, X. Dai, P. Fu, C. Fang, and J. Hu, Phys. Rev. B **96**, 115121 (2017).

[36] T.-R. Chang, S.-Y. Xu, D. S. Sanchez, W.-F. Tsai, S.-M. Huang, G. Chang, C.-H. Hsu, G. Bian, I. Belopolski, Z.-M. Yu, S. A. Yang, T. Neupert, H.-T. Jeng, H. Lin, and M. Z. Hasan, Phys. Rev. Lett. **119**, 026404 (2017).

[37] M. Yan, H. Huang, K. Zhang, E. Wang, W. Yao, K. Deng, G. Wan, H. Zhang, M. Arita, H. Yang, Z. Sun, H. Yao, Y. Wu, S. Fan, W. Duan, and S. Zhou, Nat. Commun. **8**, 257 (2017).

[38] K. Zhang, M. Yan, H. Zhang, H. Huang, M. Arita, Z. Sun, W. Duan, Y. Wu, and S. Zhou, Phys. Rev. B **96**, 125102 (2017).

[39] H. Yang, M. Schmidt, V. Süss, M. Chan, F. F. Balakirev, R. D. McDonald, S. S. P. Parkin, C. Felser, B. Yan, and P. J. W. Moll, New J. Phys. **20**, 043008 (2018).

[40] F. Fei, X. Bo, P. Wang, J. Ying, J. Li, K. Chen, Q. Dai, B. Chen, Z. Sun, M. Zhang, F. Qu, Y. Zhang, Q. Wang, X. Wang, L. Cao, H. Bu, F. Song, X. Wan, and B. Wang, Adv. Mater. **30**, 1801556 (2018).

[41] O. Pavlosiuk and D. Kaczorowski, Sci. Rep. **8**, 11297 (2018).

[42] F. Liu, J. Li, K. Zhang, S. Peng, H. Huang, M. Yan, N. Li, Q. Zhang, S. Guo, X. Lü, P. Cai, L. Yin, S. Zhou, W. Duan, J. Shen, and W. Yang, Sci. China: Phys., Mech. Astron. **62**, 48211 (2019).

[43] C. Xu, B. Li, W. Jiao, W. Zhou, B. Qian, R. Sankar, N. D. Zhigadlo, Y. Qi, D. Qian, F.-C. Chou, and X. Xu, Chem. Mater. **30**, 4823 (2018).

[44] B. Ghosh, D. Mondal, C.-N. Kuo, C. S. Lue, J. Nayak, J. Fujii, I. Vobornik, A. Politano, and A. Agarwal, Phys. Rev. B **100**, 195134 (2019).

[45] M. Emirdag, G. L. Schimek, W. T. Pennington, and J. W. Kolis, J. Solid State Chem. **144**, 287 (1999).

[46] P. E. Blöchl, Phys. Rev. B **50**, 17953 (1994).

[47] G. Kresse and J. Furthmüller, Comput. Mater. Sci. **6**, 15 (1996).

[48] G. Kresse and J. Furthmüller, Phys. Rev. B **54**, 11169 (1996).

[49] H. J. Monkhorst and J. D. Pack, Phys. Rev. B **13**, 5188 (1976).

[50] J. Heyd, G. E. Scuseria, and M. Ernzerhof, J. Chem. Phys. **118**, 8207 (2003).

[51] N. Marzari and D. Vanderbilt, Phys. Rev. B **56**, 12847 (1997).

[52] I. Souza, N. Marzari, and D. Vanderbilt, Phys. Rev. B **65**, 035109 (2001).

[53] N. Marzari, A. A. Mostofi, J. R. Yates, I. Souza, and D. Vanderbilt, Rev. Mod. Phys. **84**, 1419 (2012).

[54] M. P. L. Sancho, J. M. L. Sancho, J. M. L. Sancho, and J. Rubio, J. Phys. F **15**, 851 (1985).

[55] Q. Wu, S. Zhang, H.-F. Song, M. Troyer, and A. A. Soluyanov, Comput. Phys. Commun. **224**, 405 (2018).

[56] B.-J. Yang and N. Nagaosa, Nat. Commun. **5**, 4898 (2014).

[57] R. Yu, X. L. Qi, A. Bernevig, Z. Fang, and X. Dai, Phys. Rev. B **84**, 075119 (2011).

[58] T. Zhang, Y. Jiang, Z. Song, H. Huang, Y. He, Z. Fang, H. Weng, and C. Fang, Nature **566**, 475 (2019).

[59] T. Zhang, L. Lu, S. Murakami, Z. Fang, H. Weng, and C. Fang, Phys. Rev. Research **2**, 022066(R) (2020).